Finite element modelling of the competition between shear bands in the early stages of thrusting: Strain localization analysis and constitutive law influence

J. D. BARNICHON & R. CHARLIER
Département MSM, Université de Liège, 6 Quai Banning, 4000 Liège Belgium

Abstract: Finite element simulation of a sandbox model of thrusting is performed using large strain analysis and two different non-associated elastoplastic constitutive laws (namely Drücker–Prager and Van Eekelen criteria). The analysis of strain localization using the Rice bifurcation criterion coupled with a kinematic indicator shows that, in the early stages of imbricated thrusting, the development of major shear bands can be influenced by some competition with second order bands. The influence of the vertical/horizontal stress ratio is checked, as well as the influence of Lode angle in the constitutive law. Significant differences are found between a classical plasticity criterion (Drücker–Prager) and a more realistic one (Van Eekelen) regarding the resistance of the model and the stress paths. These differences may result in erroneous fault type prediction.

Sandbox experiments have been used extensively for many years to assist structural interpretation and validation of tectonic models. Main interests of this method come from the very large range of initial geometries which can be investigated and from the large amount of strain which can be applied. Physical parameters obtained are mainly displacement fields at different stages, especially since non destructive methods are used, e.g. X-ray tomography (Colletta *et al.* 1991).

The finite element method is also an attractive method for geological modelling as it enables computation in several parameters, examples of which are displacement, strain and stress fields, and also more recently strain localization analysis. Moreover it allows the explicit choice of mechanical characteristics, constitutive laws and boundary conditions. Abilities of the finite element method for the investigation of strain localisation along shear bands and particularly thrusting mechanism have already been shown, see, for example, Mäkel & Walters (1993).

The present paper aims to show the relative influence of the constitutive law in the results and also to analyse information obtained from localization analysis.

In the first part, some theoretical considerations are presented: basics of the large strain formulation used and principle of the finite element method are given; the choice of a representative constitutive law for sand between Mohr–Coulomb, Drücker–Prager and Van Eekelen models is discussed; a short literature overview of the strain localization analysis performed in finite element method is presented; eventually the localisation analysis used in the present paper is detailed.

The second part is mainly concerned with the simulation of a sandbox model of thrusting carried out with the LAGAMINE finite element code. Early stages of thrust development are analysed in a first simulation in the light of the Rice bifurcation criterion and of a kinematic indicator of localization. A non-associated Drücker–Prager yield criterion is used. A remeshing procedure is also performed in this first simulation to increase the applied loading value. The influence of the vertical/horizontal stress ratio is checked in a second simulation. The last simulation investigates the influence of the third stress invariant in the plasticity surface definition using a more sophisticated yield criterion, namely the Van Eekelen.

In the last part, finite element simulation results obtained are compared with some experiments performed on sandbox models.

Theory

Simulation of geological deformation often requires taking into account the occurrence of large strains, i.e. strains larger than 1–5%. Highlights of the large strain finite element formulation are presented. These concepts have been applied for one decade to metal forming processes. They have been presented in a set of papers, see for instance Cescotto (1989) and Cescotto *et al.* (1989). The choice of a constitutive law for sand and the strain localization analysis are also discussed.

Large strains

Modelling of a solid undergoing large strains can be described in different configurations: the initial

From Buchanan, P. G. & Nieuwland, D. A. (eds), 1996, *Modern Developments in Structural Interpretation,Validation and Modelling*, Geological Society Special Publication No. 99, pp. 235–250.

unstrained configuration, the current deformed configuration, or any other configuration between the initial and the present state. In the present work, equilibrium is expressed using the updated Lagrangian formulation in the current configuration. The Cauchy stress tensor is adopted. The constitutive relation can be written in a general form

$$\overset{\nabla}{\underline{\sigma}} = fct(\underline{D}, \underline{\sigma}) \tag{1}$$

It is related to the symmetric part $\underline{D}$ of the velocity gradient $\underline{L}$

$$\underline{D} = \frac{1}{2}\ (\underline{L} + \underline{L}^T) = \frac{1}{2}\left(\frac{\partial \underline{v}}{\partial \underline{x}} + \frac{\partial \underline{v}^T}{\partial \underline{x}}\right) \tag{2}$$

where x are the current co-ordinates and $\underline{v}$ are the current velocities.

The Jaumann objective stress rate is adopted

$$\overset{\nabla}{\underline{\sigma}} = \dot{\underline{\sigma}} - \underline{\omega}\underline{\sigma} - \underline{\sigma}\underline{\omega}^T \tag{3}$$

with the rotation rate ω which is equal to the anti-symmetric part of the velocity gradient $\underline{L}$

$$\underline{\omega} = \frac{1}{2}\ (\underline{L} - \underline{L}^T) = \frac{1}{2}\left(\frac{\partial \underline{v}}{\partial \underline{x}} - \frac{\partial \underline{v}^T}{\partial \underline{x}}\right) \tag{4}$$

It must be noticed that equation (2) cannot generally be integrated, therefore strains associated with the Cauchy stress tensor do not exist. When the strains produced by the whole loading processes analysed later in this paper, the natural strain tensor will be used

$$\underline{G} = \ln \underline{U} \tag{5}$$

where the stretching tensor $\underline{U}$ is obtained by the polar decomposition of the transformation Jacobian $\underline{F}$ from the initial to the current configuration, $\underline{R}$ being the rigid body rotation tensor

$$\underline{F} = \underline{R}\underline{U} \tag{6}$$

This strain measure $\underline{G}$ coincides with the integral of (2) in principal axis if they remain unchanged.

Finite element principle

The finite element method is based on the virtual work principle (Zienckiewicz & Taylor 1988). It assumes that the local volume and surface equilibrium conditions are verified if the virtual work equation

$$\int_v \underline{\sigma} : \underline{\delta\varepsilon}\ dv = \int_v \rho \underline{g}_I^T\, \underline{\delta u}\ dv + \int_a \underline{t}^T\, \underline{\delta u}\ da \tag{7}$$

where $\underline{\delta\varepsilon}$: virtual strain
ρ: volumic mass
$\underline{g}_I$: gravity acceleration
$\underline{t}$: surface forces

is satisfied for any virtual displacement $\underline{\delta u}$. The large transformation effect is here taken into account because the volume integral is computed in the current configuration. The virtual strains are

$$\underline{\delta\varepsilon} = \frac{1}{2}\left(\frac{\partial \underline{\delta u}}{\partial \underline{x}} + \frac{\partial \underline{\delta u}^T}{\partial \underline{x}}\right) \tag{8}$$

The virtual work equation is computed in the current configuration at the end of each load step.

In the finite element method, equation (7) is only verified for a limited number of virtual displacement fields associated with the mesh degrees of freedom. Hereafter isoparametric finite elements with eight nodes (parabolic displacement field) and four Gauss integration points (under-integration of the virtual work) are used.

The virtual work equation is non-linear since it is using an integration on a configuration and on stresses which are defined at the end of the step and unknown at the beginning of the step. This non linearity is solved using the Newton Raphson iterative method.

Constitutive laws for geomaterials

Regarding the choice of a representative constitutive law for sand, the question is open as the actual behaviour of the sand under small confining pressure is not very well known. However if we consider mainly internal frictional characteristics of sand, several constitutive models can be put forward. In order to avoid confusion, the choice of stress sign follows geomechanics convention, i.e. compressive ones are counted as positive.

Mohr–Coulomb criterion

The well known Mohr–Coulomb failure criterion expresses a linear relationship between the shear stress τ and the normal stress σ_n acting on a failure plane

$$\tau = C + \sigma_n \tan \phi \tag{9}$$

Parameters ϕ (friction angle) and C (cohesion) are commonly identified from conventional triaxial compression tests (i.e. $\sigma_1 > \sigma_2 = \sigma_3$) on cylindrical specimens by construction of the Mohr envelope at failure. Therefore the friction angle ϕ found corresponds to a compressive stress path, it can be called 'friction angle in compression' and noted ϕ_C. Mohr–Coulomb theory assumes that this friction angle does not depend on the stress path, for instance friction angles in compression ϕ_C and in

tension ($\sigma_1 < \sigma_2 = \sigma_3$) ϕ_E are equal (Desai & Siriwaradane 1984).

However this model is not convenient to use in numerical analysis mainly because its representation in the principal stress space (σ_1, σ_2, σ_3) is an irregular hexagonal pyramid leading to singularities (the normal of the surface at intersection lines is not unique). This feature can be seen on Fig. 1 which represents the trace of this plasticity surface in the deviatoric plane.

Drücker–Prager criterion

An alternative solution to overcome this difficulty has been proposed by Drücker & Prager (1952) who defined the yield function F using a linear relationship between the first stress tensor invariant and the second deviatoric stress tensor invariant

$$F = \sqrt{II_{\hat{\sigma}}} - mI_\sigma - k = 0 \tag{10}$$

with

$$I_\sigma = \sigma_{kk} \tag{11}$$

$$II_{\hat{\sigma}} = \frac{1}{2}\hat{\sigma}_{ij}\hat{\sigma}_{ij} \quad \text{where } \hat{} \text{ represents the deviatoric part of the tensor} \tag{12}$$

In the principal stress space, the plasticity surface becomes a cone which is much easier to use in numerical algorithms. The trace of this plasticity surface on the Π plane (i.e. the deviatoric plane) is then a circle (see Fig. 1).

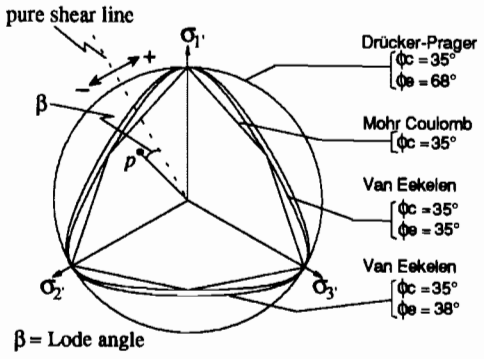

Fig. 1. Limit surface for Mohr–Coulomb, Drücker–Prager and Van Eekelen models in the deviatoric plane. Note that Drücker–Prager criterion can either be chosen circumscribed or inscribed to the Mohr–Coulomb. Lode angle $\beta = 30°$ with respect to the pure shear line corresponds to triaxial compression and $\beta = -30°$ to triaxial extension. Van Eekelen model is a smoothing of Mohr–Coulomb criterion which can respect both compression and extension friction angles, but which can also take different values for these two angles.

However this quite simple criterion has one main disadvantage very often neglected and which must be outlined: it does not incorporate a dependence on the third stress invariant and thus on the Lode angle β

$$\beta = -\frac{1}{3}\sin^{-1}\left[\frac{3\sqrt{3}}{2}\frac{III_{\hat{\sigma}}}{II_{\hat{\sigma}}^{3/2}}\right] \text{ with } III_{\hat{\sigma}} = \frac{1}{3}\hat{\sigma}_{ij}\hat{\sigma}_{jk}\hat{\sigma}_{ki} \tag{13}$$

which is the angular position of the projection p of a stress state on the Π plane with respect to the pure shear line (see Fig. 1). From Fig. 1, β factor is in the range $-30°$ to $30°$ triaxial compressive stress paths correspond to $\beta = 30°$, whereas triaxial extensive ones correspond to $\beta = -30°$. Consequently mobilized friction angles are either over or underestimated depending on the stress path, leading to discrepancy in the results obtained (Schweiger 1994): a compression cone (i.e. a circumscribed cone) induces high friction angle for extension paths, whereas the internal cone leads to low equivalent friction angles.

This can be illustrated considering the case where the compression cone is chosen:

– identification of parameters m and k on the Mohr envelope as a function of internal friction angle in compression ϕ_C and cohesion C then gives (Desai & Siriwaradane 1984)

$$m = \frac{2\sin\phi_C}{\sqrt{3}(3 - \sin\phi_C)}, \quad k = \frac{6C\cos\phi_C}{\sqrt{3}(3 - \sin\phi_C)} \tag{14}$$

– with the definition of reduced radius r

$$r = \frac{II_{\hat{\sigma}}}{I_\sigma}, \tag{15}$$

expressions of the reduced radius in compression (r_C) and in extension (r_E) for triaxial tests can be deduced from Mohr circle and intrinsic curve, leading to

$$r_C = \frac{1}{\sqrt{3}}\left(\frac{2\sin\phi_C}{3 - \sin\phi_C}\right), \quad r_E = \frac{1}{\sqrt{3}}\left(\frac{2\sin\phi_E}{3 + \sin\phi_E}\right) \tag{16}$$

which, putting $r_E = r_C$ as the radius is constant, gives a simple relation between ϕ_C and ϕ_E. For instance if a value $\phi_C = 35°$ is chosen, then ϕ_E takes the value $\phi_E = 68°$ which is much higher than ϕ_C and far from being realistic.

This can also be seen graphically on Fig. 1: the Drücker–Prager cone is a only a poor representation of the Mohr–Coulomb hexagon as one can either chose a circumscribed cone (Fig. 1), an inscribed cone, or any intermediate choice between the last two. None of these choices is actually satisfactory for any stress path.

Classically, the flow rule is associated if $G = F$, where G represents the flow potential, which implies that the plastic flow is normal to the yield surface and leads to an excess of dilatancy. A non-associated flow rule G can be defined in an identical fashion as the yield function F (see relations (10) and (14)) simply substituting ϕ by ψ in equation (14), ψ being the dilatancy angle.

Van Eekelen criterion

More sophisticated models can be built from the Drücker–Prager cone by introduction of a dependence on the Lode angle β in order to match more closely Mohr–Coulomb criterion. Several models of this type have been described, including the Matsuoka–Nakaï and Van Eekelen. The Van Eekelen plasticity criterion (Van Eekelen 1980)

$$F = aI_\sigma(1 - b \sin 3\beta)^n - \sqrt{II_\delta} = 0 \qquad (17)$$

allows an independent choice for ϕ_C and ϕ_E via coefficients a and b

$$b = \frac{\left(\frac{r_C}{r_E}\right)^{1/n} - 1}{\left(\frac{r_C}{r_E}\right)^{1/n} + 1}, \quad a = \frac{r_C}{(1+b)^n} \qquad (18)$$

where r_C and r_E are given by equation (16). The exponent n actually controls the convexity of the yield surface, condition generally required in classical plasticity framework. A parametric study showed that the convexity is always verified with $n = -0.229$ provided that $\phi_E \geq \phi_C$ which is a realistic assumption for sand.

The trace of this plasticity surface in the Π plane is shown on Fig. 1. Such a model is actually a smoothing of the Mohr–Coulomb hexagon, but it fits much better the Mohr–Coulomb criterion and experimental data than the Drücker–Prager failure criterion (Matsuoka & Nakai 1982). Moreover this criterion allows for an independent choice of friction angles in compression and extension (see Fig. 1 with $\phi_C = 35°$, $\phi_E = 38°$).

As for Drücker–Prager model, the flow rule G can either be defined associated ($G = F$) or non-associated ($G \neq F$).

A noteworthy feature of this more sophisticated criterion is that no additional material parameters are required compared to a Drücker–Prager criterion. Simply the friction angle in extension ϕ_E is explicit here whereas it was implicit in the Drücker–Prager criterion.

Contact friction law

For rigid wall/sand contacts, the Coulomb friction law (Charlier & Cescotto 1988) is generally considered

$$F = \sqrt{\tau_S^2 + \tau_T^2} - C - \mu P = 0 \qquad (19)$$

where μ is the friction coefficient, C the cohesion, P the contact pressure, τ_S and τ_T the shear stresses. The corresponding boundary condition is implemented using interface finite elements (Charlier & Cescotto 1988; Charlier & Habraken 1990; Cescotto & Charlier 1993).

Bifurcation and shear band localization of deformation

Bifurcation phenomenon can be viewed as alternative stress and strain paths under a given loading condition, which traduces mathematically by the loss of uniqueness of the solution. Strain localization along shear bands, which represents one potential bifurcation mode, is known to occur frequently in frictional materials.

The study of problems involving shear band localization by the finite element method faces several difficulties.

(1) The constitutive relation considered in the finite element model must allow for bifurcation. For elastoplastic laws it has been demonstrated that localization requires at least either a hardening/softening law or a non-associated one (Rice 1976). Bifurcation can occur at the peak load for strain softening models, but also in the hardening range if a non-associated law is considered (Rice 1976). This last feature has actually been observed in experiments on dense sands (Desrues 1984) in which localization occurs before the stress peak.

(2) Unique solution at the bifurcation point must be determined. If strain softening is introduced in a classical continuum model, the condition for localization coincides with the loss of ellipticity of equations. As a result, the finite element solution shows pathological mesh dependence because the band thickness is undetermined (De Borst 1993). In classical finite element computations, the band thickness has usually the size of an element (Ortiz *et al.* 1987; De Borst & Sluys 1991). This difficulty is still a very active field of research, and up to now 3 main approaches have been developed to overcome this problem by introduction of an internal length scale in the problem, which causes the problem to remain well-posed at localization: higher order strain gradients (De Borst 1992) introduced in the constitutive equation; non local constitutive relations in which some variables are taking into account the spatial variation of strain and micro-polar (or Cosserat) continuum in which rotational degrees of freedom are added in the element formulation (De Borst 1993). However a meaningful physical interpretation for the internal

scale has still not been found. Therefore identification of this parameter is an open question and obviously the value chosen in numerical analyses is arbitrary.

(3) The post-bifurcation behaviour must be correctly computed, and here several approaches have been described in literature. They aim to provide an improved strain computation in shear bands (which are characterized by high strain gradients): mesh refinement around the band, higher order shape functions of finite elements (Ortiz *et al.* 1987) are some of the possible strategies.

The simulations presented in this paper are performed in the framework of classical continuum theory. Non-associated constitutive relations are considered to allow for bifurcation. A local analysis of strain localization is performed at the element level based on a criterion for shear band bifurcation (Rice 1976; Wang 1993). A kinematic indicator is also found useful to follow accurately the evolution of strain localization, especially initiation. An adaptive remeshing technique has also been used here to avoid large distortion of elements and thus enables the modelling to be carried out until larger loading values. All these features are described more explicitly in the next three sections.

Local shear band bifurcation criterion

The Rice criterion (Rice 1976) analyses the stress state and investigates the possibility of a bifurcation by formation of a shear band in the stress and strain paths. The theoretical scheme of a shear band is presented in Fig. 2. Its development has become classical. It is based on a kinematic condition, a static condition and on the constitutive equation. We note ^{0} variables outside the band and ^{1} variables inside the band.

The static condition expresses the surface equilibrium at the interface between the inner and outer band

$$n_j(\sigma^1_{ij} - \sigma^0_{ij}) = 0 \tag{20}$$

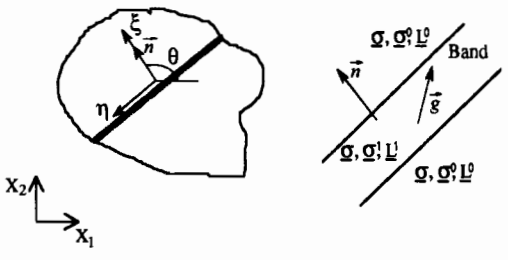

Fig. 2. Theoretical scheme of a shear band.

The kinematic condition expresses the strain jump across the band interface by a dilatant strain jump and a shear strain jump, but without any longitudinal strain jump

$$\underline{L}^1 = \underline{L}^0 + \vec{g} \otimes \vec{n} \tag{21}$$

where $\underline{L}$ is the velocity gradient, $\underline{n}$ is the normal to the band, and $\underline{g}$ is a vector describing the band mode (from shearing to dilatation, from mode II to mode I).

The third equation introduced in the Rice criterion is the constitutive law. For an elastoplastic or an elastic law, one has

$$\mathring{\underline{\sigma}} = \underline{\underline{D}}\,\underline{L} \tag{22}$$

where the constitutive tangent tensor $\underline{\underline{D}}$ includes the objective stress rate correction, usually the Jaumann one.

For an elastoplastic law this equation becomes

$$\mathring{\underline{\sigma}} = \underline{\underline{C}}^{ep}\,\frac{1}{2}(\underline{L} + \underline{L}^T) + \underline{\sigma}\,\frac{1}{2}(\underline{L} - \underline{L}^T)^T + \frac{1}{2}(\underline{L} - \underline{L}^T)\,\underline{\sigma} \tag{23}$$

It is important to point out that equation [23] assumes loading or unloading stress paths. The obtained bifurcation criterion is therefore a lower bound (if the loading tensor is used) and not an exact one.

Introducing (23) into (20) and (21), one obtains a third order equation system which unknowns are the components of the $\underline{g}$ vector. The trivial solution $\underline{g} = 0$ is always possible but it means that not shear band can appear. The condition $\underline{g} \neq 0$ can be transformed in a fourth order equation in $\tan(\theta) = t$, with θ being the angle between the band normal and the x axis (Wang 1993)

$$at^4 + bt^3 + ct^2 + dt + e = 0 \tag{24}$$

At the beginning of loading, this equation does not have any real solution. After some load steps, the first real solution is a double one. More generally one or two solutions are possible.

The Rice bifurcation criterion indicates the possibility of a shear band appearance from a local stress point of view. It actually does not show developing shear bands effectively. From a practical point of view, this criterion is computed at every iteration for all integration points.

Kinematic indicator of localization

Analysis of the strain field can actually show strain localization. The simplest analysis of a shear band apparition is based on the visualization of the cumulated equivalent strain map

$$\varepsilon_{eq} = \sqrt{\hat{G}_{ij}\hat{G}_{ij}} \tag{25}$$

where G is given by relation (5). However, maps of this type show well achieved shear bands when localization has strongly developed, but does not give the possibility of showing early stages of localization.

In order to overcome this deficiency, a kinematic scalar indicator α can be defined, based on some propositions by Vilotte *et al.* (1990)

$$\alpha = \frac{\Delta\varepsilon_{eq}\,\Delta t}{\varepsilon_{eq}} \tag{26}$$

where Δt is the numerical time step increment and $\Delta\varepsilon_{eq}$ is the incremental deviatoric strain rate.

This indicator represents the incremental equivalent strain related to cumulated equivalent strain. It enables localization to show much earlier than relation (26).

Adaptive remeshing

Under the intense shearing occurring in shear bands, elements are distorted and quickly fail. Remeshing techniques are powerful methods to overcome this difficulty and to enable the simulation to carry on.

Adaptive remeshing procedures have been initially developed in fluid dynamics and in metal forming modelling (see for example Cheng (1988) and Habraken & Cescotto (1990)). The general procedure is in three steps:

(1) evaluation of the remeshing need, based on some indicator. One can use an error estimate algorithm (Zienkiewicz & Zhu 1987) or a localization indicator. In the present case, remeshing is based more arbitrarily on a convergence criterion.
(2) creation of a new mesh, based on a meshing algorithm with variable element density in order to produce a mesh adapted to the deformations to be modelled.
(3) transfer of state variables (mainly stresses) and kinematics variables (nodal velocities) from the old mesh to the new one using the following interpolation algorithm

$$a(\underline{x}^J) = \begin{cases} a(\underline{x}^i) & \text{if } r_{iJ} \le r_0 \\ \dfrac{\sum_{\text{NINT}} \dfrac{a(\underline{x}^i)}{r_{iJ}^p}}{\sum_{\text{NINT}} \dfrac{1}{r_{iJ}^p}} & \text{if } r_{iJ} > r_0 \end{cases} \tag{27}$$

where a is the quantity to transfer, ^{i} relates to the old mesh and ^{J} to the new one, $\underline{x}$ are co-ordinates, r_{iJ} is the distance between point ^{i} and ^{J}, p is the order of interpolation and the summation sign indicates a summation over all integration points of the old mesh.

It must be pointed out that after these operations, the simulation re-start is always slightly difficult because the new configuration is never perfectly equilibrated. This difficulty appears as a small discontinuity on the load/displacement curve at remeshing points (indicated with arrows on Fig. 5).

Application: simulation of sandbox thrusting model

Geometry, boundary conditions and discretization

Plane strain two dimensional simulation of thrusting in a sandbox model has been performed using the LAGAMINE finite element code. The basic model consists of a 20 cm length/1.4 cm thick horizontal sand layer laying on a horizontal rigid basement (see Fig. 3). The right hand side of the model is horizontally fixed. A horizontal displacement u is applied to the rigid wall at the left hand side of the model using incremental displacements Δu.

Contact between rigid wall/basement and sand is managed via 58 frictional interface elements. The basal contact actually represents a basal detachment plane whose position is given a priori, i.e. which represents a major rheological discontinuity.

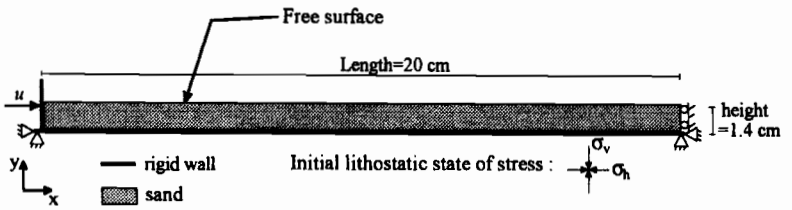

Fig. 3. Geometry and boundary conditions for the basic model.

Discretization of the sand massif is achieved using 400 elements (0.4 × 0.175 cm).

The convergence criterion for the Newton–Raphson iterative method is based on a displacement and a force criterion. An adaptive step size method based on convergence criteria is used in which size of loading increments is allowed to vary between 10^{-5} and 10^{-1} cm.

A balanced lithostatic stress field is introduced in the initial conditions of the model. Considering the orientation of the y axis shown in Fig. 3, vertical stresses σ_v are given by

$$\sigma_v = -\rho g_r y \tag{28}$$

and horizontal stresses σ_h are defined by the ratio K_0 with

$$K_0 = \frac{\sigma_h}{\sigma_v} \tag{29}$$

Physical parameters

Three sets of numerical simulations have been carried out. Rigid wall/sand contacts are simulated using non-associated Coulomb law; the parameters are given in Table 1. A non-associated elastoplastic law without dilatancy ($\psi = 0°$) and without hardening/softening is chosen for the sand in all three sets of experiments. A Drücker–Prager (DP) criterion is considered for experiments 1 and 2 whereas a Van Eekelen (VE) criterion is chosen for experiment 3. The major difference between those two models comes mainly from the friction angle in extension ϕ_E (see Table 1).

Results

All the maps presented hereafter represent only the left part of the model as in the right part almost nothing occurs (far field limit).

Simulation 1 (sm1): initial model

In this simulation, a remeshing procedure has been used twice in order to carry on simulation when convergence could no longer be achieved, respectively at $u = 0.5$ cm and $u = 0.8$ cm, u being the displacement applied to the rigid wall. Therefore this simulation consists of three consecutive runs from which several computed results can be analysed.

Equivalent strain. Figure 4 represents isovalue maps of the evolution of equivalent strain cumulated (see equation [25]) over each remeshing phase (i.e. between 0 and 0.5 cm, 0.5 and 0.8 cm, 0.8 and 0.9 cm respectively), i.e. equivalent strain is reset to zero at the begin of each remeshing. As this deformation measurement is cumulated over one run, it gives rather rough indication of what actually happens within the model. However it clearly shows the formation of three main shear bands.

(a) From $u = 0$ to 0.5 cm (Fig. 4a), a major synthetic reverse shear band (called band n. 1) develops in front of the rigid wall. This band is linked to the free surface but does not reach the bottom part of the model.

(b) From $u = 0.5$ to 0.8 cm (Fig. 4b), a second major synthetic reverse shear band (called band n. 2) develops in front of the band n. 1, with the same orientation than the latter. However an antithetic reverse shear band (band n. 3) has also developed to a lesser extent; these two reverse faults define a pop-up structure. Clearly band n. 1 has been inactive during this stage.

(c) From $u = 0.8$ to 0.9 cm (Fig. 4c), most of the deformation is achieved along the band n. 2 in which cumulated equivalent strain reaches locally 30%. Little deformation is achieved along band n. 3, and a new antithetic reverse band (band n. 4) is developing on the left of band n. 3. The close left boundary does not allow to argue for relevance of this latter band.

Strain localization analysis. Localization of deformation can be analysed using information obtained from the Rice criterion and from the kinematic indicator α. It is also interesting to incorporate in this analysis the force/displacement curve given in Fig. 5.

The localization of deformation along band n. 1 is quite clear, four phases can be distinguished.

(1) From $u = 0$ to 0.247 cm

Table 1. *Physical parameters for the three sets of experiments*

	Contact		Sand								
Simulation	C (Pa)	μ	Law type	E (Pa)	ν	C (Pa)	ϕ_C (°)	ϕ_E (°)	ψ (°)	ρ (kg/m³)	K_0
1	0	1	DP	$5\ 10^4$	0.2	20	35	68	0	2250	0.25
2	0	1	DP	$5\ 10^4$	0.2	20	35	68	0	2250	1.0
3	0	1	VE	$5\ 10^4$	0.2	20	35	35	0	2250	0.25

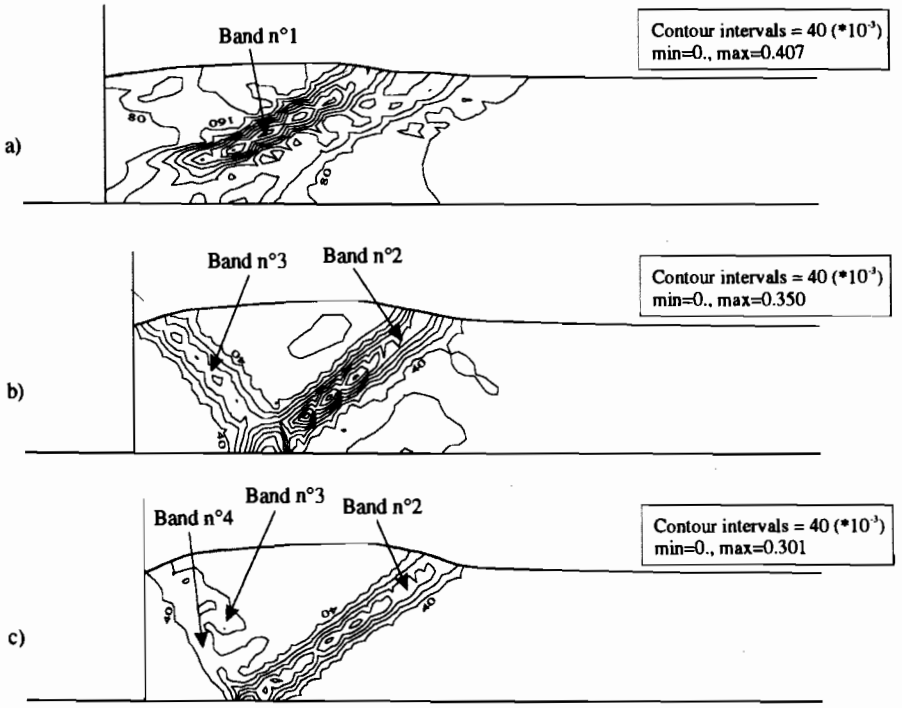

Fig. 4. Isovalues maps of cumulated equivalent strain for each respective mesh of simulation 1. (**a**) $u = 0$ to 0.5 cm: mainly the synthetic reverse shear band n°1 develops.(**b**) $u = 0.5$ to 0.8 cm: the synthetic reverse shear band n°2 and in a lesser extent the antithetic shear band n°3 have developed during this phase. (**c**) $u = 0.8$ to 0.9 cm: mainly the band n°2 is active, band n°3 is only a little active. A new antithetic reverse shear band (n°4) starts to develop.

The loading curve slope is positive (Fig. 5), the Rice criterion and the kinematic indicator give rather diffuse information. However as the imposed displacement gets closer to $u = 0.247$ cm, the slope of the loading curve decreases progressively and the kinematic indicator shows that localisation starts along band n. 1.

(2) From $u = 0.247$ to 0.257 cm

The loading curve slope is negative (Fig. 5) corresponding to an unloading phase. It is worth mentioning that such phenomenon can be referred to as structural (or geometrical) softening because no hardening/softening is included in the constitutive equation. Therefore in the model, a global 'softening' response does not even require introduction of softening in the constitutive law.

The Rice criterion (Fig. 6a) is represented at each potentially bifurcated point using arrows which indicate the potential two directions for bifurcation (computed from θ given by equation [24]). During this phase, the two localization indicators give almost the same result, i.e. all the deformation which occurs in the model is localized along band n. 1 (see Figs 6a and b). This phase corresponds to an active phase of localization. One must point out that during this phase of active localization, numerical convergence could only be achieved with very small loading increments ($\approx 10^{-5}$ cm).

(3) From $u = 0.257$ to 0.29 cm

The loading curve slope becomes positive again (Fig. 5). The Rice indicator gives again a rather diffuse information, whereas the kinematic indicator shows that two 'second order' shear bands appear in the basal area and compete with the main band n. 1 ('second order' refers to the point that these bands develops from a major band where almost the whole strain is achieved). One of these second order shear is shown at $u = 0.27$ cm on Fig. 6c. These second order bands indicate a clockwise rotation of the base of the main shear band n. 1.

(4) For $u > 0.29$ cm

As the applied displacement u increases further, band n. 2 and 3 develop. Formation of these 2 faults does not appear in a very active localization phase as band n. 1: for example see Fig. 5 where the negative slope phase at $u = 0.325$ cm is quite reduced compared with the one at $u = 0.25$ cm.

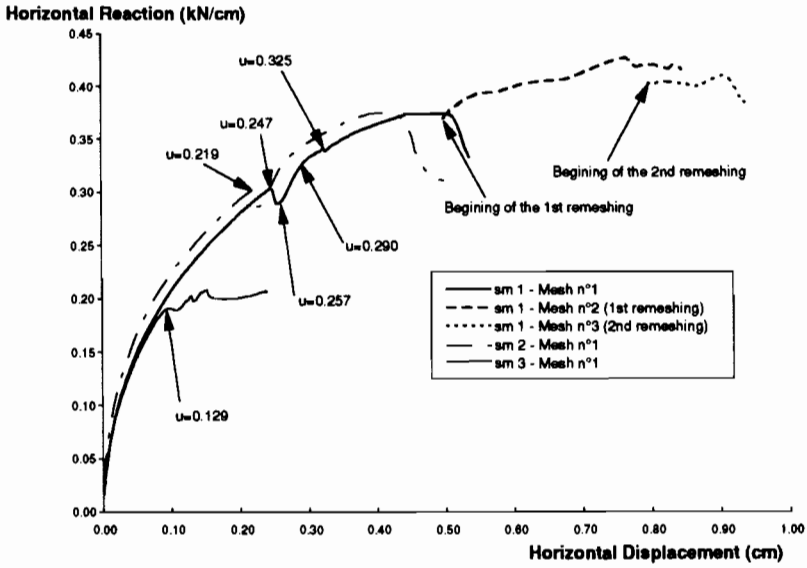

Fig. 5. Plot of the horizontal displacement versus horizontal reaction for the three simulations. For sm1 and sm2, bifurcation appears as an unloading phase at $u = 0.247$ and 0.219 cm respectively. For sm3, bifurcation occurs earlier, i.e. at $u = 0.129$ cm. Note also that prior localization, the reaction is lower for sm3 compared with sm1 and sm2.

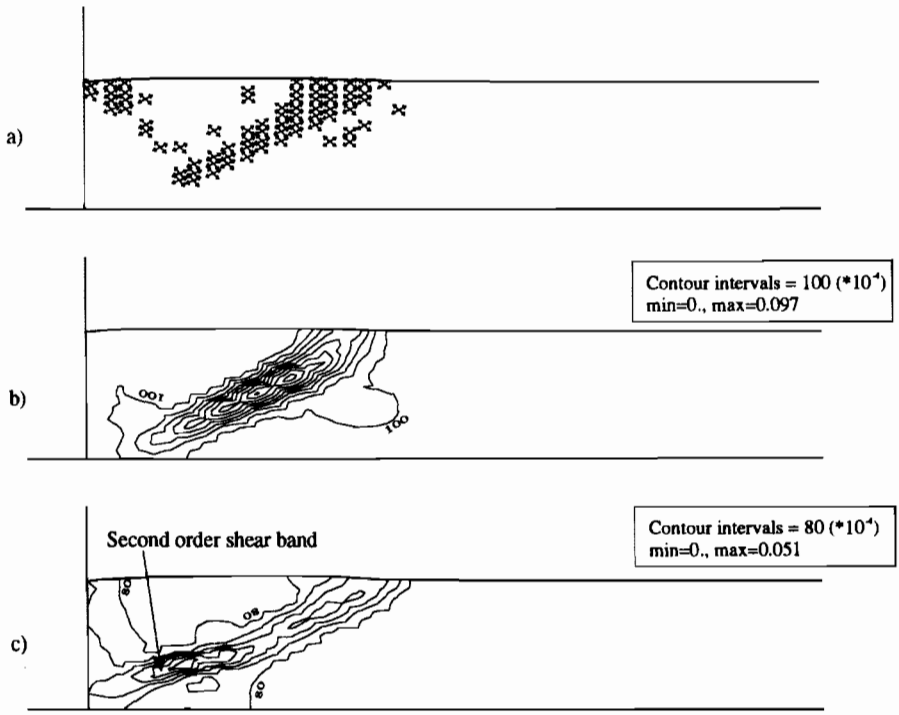

Fig. 6. Strain localization analysis for simulation 1. (**a**) Rice bifurcation at $u = 0.25$ cm: the two potential directions for bifurcation show localization along band n°1. (**b**) Isovalues map of the kinematic indicator α at $u = 0.25$ cm: localization occurs clearly along band n°1. Note that information is comparable to (a). (**c**) Isovalues map of the kinematic indicator α at $u = 0.27$ cm: a 'second order band' is developing at the bottom part of the model and indicates a clockwise rotation of band n°1.

The 'fault activity' (which is represented by the kinematic indicator α) shows non negligible variations as bands n. 2 and 3 are initiated. It actually illustrates transient faulting phases (i.e. which do not accommodate important deformation) and shear band competition. It also shows locking of some major bands (see for example band n. 1 for $u > 0.5$ cm). A sketch of the overall fault activity between $u = 0$ and $u = 0.9$ cm is given in Fig. 7. In this diagram, locations referred as 'low fault activity' are sketched to record that localization has occurred in these areas at some time during the loading process. No localisation is actually occurring at the respective loading stage they are sketched.

This competition between bands is likely to be partly induced by the elastoplastic parameters chosen, especially regarding softening: as no hardening/softening is taken into account in the constitutive relation, the material remains 'virgin' or unweakened even when it experiences deformation. However such phenomenon of competition between shear bands has also been observed in experiments performed on sand samples (Desrues 1984), i.e. on strain hardening/softening materials.

The localization analysis enables study at a small loading scale where localization actually occurs and allows visualization of competition phenomenon between bands as well as second order faults, phenomenon which were not seen with classical equivalent strain maps.

Shear band orientation. Principal stress tensors are plotted on Fig. 8a. Maximum principal stress (σ_1) directions deduced from the stress field at $u = 0.2$ cm are represented in dotted lines on Fig. 8b. Note the clockwise rotation of σ_1 direction close to the basal interface, which is induced by shear stresses on the sand/rigid basement interface.

This principal stress rotation has two main effects on orientation of shear bands, whose positions are illustrated on Fig. 8b:

- bands n. 1 and 2 exhibit concave upward shapes, the actual dip (angle with respect to horizontal) for band 1 and 2 varies vertically between 25 and 38°,
- dip for band n. 3 is approximately 46°, which is a much higher angle than for the other 2 bands.

Identical effects of basal shear stresses on shear band orientation have already been suggested by some previous authors (Mandl & Shippam 1981). This has also been verified in some finite element analysis (Makel & Walters 1993).

If angles of shear bands with respect to σ_1 direction are now considered, it is found that all the bands develop with an approximate angle $\Theta = 36°$ with respect to σ_1. This angle value is compatible with the range theoretically predicted for granular media

$$\frac{\pi}{4} - \frac{\phi}{2} \leq \Theta_{theo} \leq \frac{\pi}{4} - \frac{\phi + \psi}{4} \tag{30}$$

where the lower bound is obtained from classical Coulomb prediction and the upper bound is given by Arthur *et al.* (1977). Here with $\phi = \phi_C = 35°$ and $\psi = 0°$, equation (30) leads to

$$25.7 \leq \Theta_{theo} \leq 36.25°$$

The value obtained $\Theta = 36°$ is compatible with Θ_{theo}. If the upper bound for friction angle is

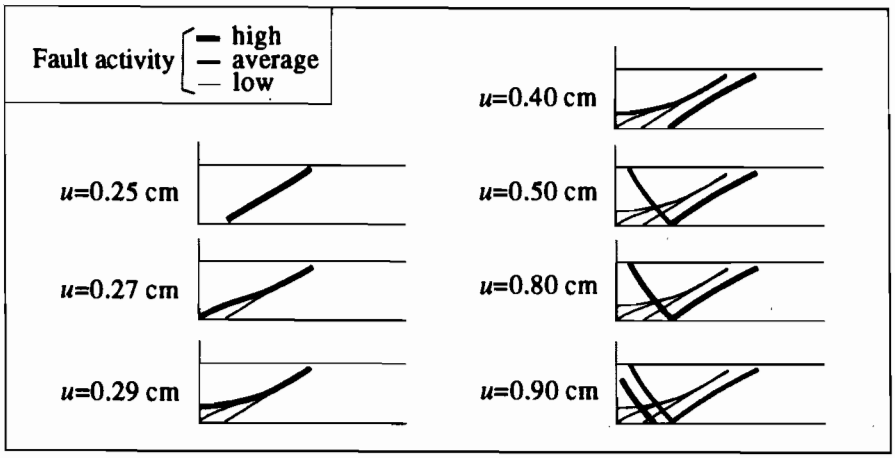

Fig. 7. Schematic relative fault activity (based on kinematic indicator α) for simulation 1.

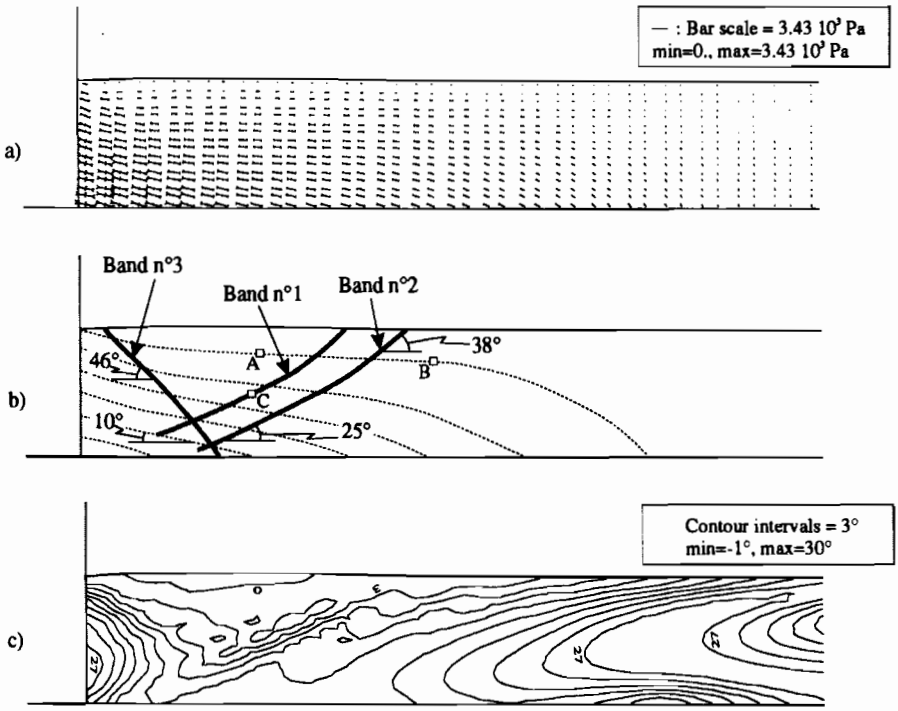

Fig. 8. Simulation 1. (**a**) Stress tensor representation at $u = 0.20$ cm, i.e. prior localization. (**b**) Dotted lines: maximum principal stress (σ_1) direction built from the stress field given in (a) at $u = 0.20$ cm; in the left part of the model, stresses are clockwise rotated due to shear stresses which develop at the model basement. Bold lines: schematic location of the future shear bands with approximate angles values at initiation (location of points A, B and C refer to Fig. 12). (**c**) Lode angle (β) isovalues map at $u = 0.25$ cm: in most of the left part, β falls in the range $-1 < \beta < 9°$, which indicates a stress path with a shearing component.

considered (i.e. $\Theta_E = 68°$), the predicted friction angle given by equation (30) is lower than the values obtained.

As expected, the thickness of the band is found to be approximately the size of one element. It must also be pointed out that no evident relation has been found to determine the position of the band. Clearly there is some competition between shear stresses on the basal interface and internal shear resistance of the material. It must be pointed out that in the early stages of localization (see Figs 6a–b), the shear band n. 1 does not initiate from the base of the model (see Figs 6a–b), whereas this is the case when no frictional interface is given in initial conditions (Makel & Walters 1993).

Lode angle. Lode angle value β (see equation (13)) indicates whether the current state of stress follows compressive ($\beta = 30°$) or extensive ($\beta = -30°$) stress paths. From the isovalue map of β presented in Fig. 8c, it is clear that Lode angle values fall in the range $-1 < \beta < 30°$ if the left part of the model is considered. As we get closer to the bands, β actually ranges between -1 and $9°$ which indicates a stress path with shear component, which is far from being purely compressive. As a result, mobilized friction angle ϕ_m deduced from the DP criterion in this part of the model is much higher than the value $\phi_C = 35°$ (see description of Drücker–Prager criterion) and ranges between 35 and 55°. Effects of this friction angle overestimation will be investigated in simulation 3 using Van Eekelen criterion.

Simulation 2 (sm2): influence of the K_0 ratio

The aim of this second simulation is only to check the influence of K_0 ratio on localisation. Therefore the difference between this simulation and sm1 comes from the K_0 value which here is equal to one, that is the initial state of stress is hydrostatic. Computations are only performed for displacement values up to $u = 0.5$ cm without remeshing.

Regarding the loading/displacement curve (see Fig. 5), one can observe that localization occurs here for an identical loading value than for sm1, i.e. approximately 0.30 kN cm^{-1}. For identical displacement values, the horizontal reaction is slightly

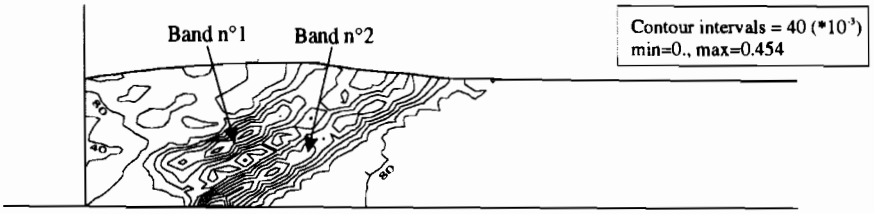

Fig. 9. Isovalues maps of cumulated equivalent strain for simulation 2 for $u = 0$ to 0.5 cm. Bands n°1 and 2 have developed as in sm1. However as localization occurred earlier in this simulation than in sm1, these 2 bands are better developed, especially band n°2 (compare with Fig. 4a at identical loading).

higher here than for sm1. This results directly from the increase of confining pressure induced by K_0 ratio. The two curves have almost identical shapes apart that localization occurs earlier in sm2 than in sm1 ($u = 0.219$ cm and $u = 0.247$ cm respectively).

Regarding displacement field and strain localization computed at the end of the simulation, direct comparison of equivalent strain at $u = 0.5$ cm between sm2 (Fig. 9) and sm1 (Fig. 4a) can be made. Few differences are found with sm1: the main difference comes actually from the band n. 2 which is markedly more developed here. This results from the earlier localization which occurs in this simulation.

Simulation 3 (sm3): influence of the Lode angle

The difference between this simulation and sm1 comes from the plasticity criterion which here is a Van Eekelen one whereas a Drücker–Prager was used in sm1. Computations are performed for displacement values up to $u = 0.22$ cm without remeshing.

Strain localization. Localization occurs earlier in this model ($u = 0.129$ cm), i.e. for lower loading values than in sm1 and sm2 (see Fig. 5). Map of the kinematic indicator a presented on Fig. 10a shows that two imbricated synthetic shear bands have started to develop in the left part of the model at $u = 0.2$ cm, which is qualitatively similar to sm1 and sm2. However the analysis of the equivalent strain map (Fig. 10b) shows that the main part of deformation (locally up to 80%) has occurred close to the basement model along a basal slip. This directly results from the mobilised friction angle ϕ_m which is lower here ($35 < \phi_m < 40°$) than in sm1 and sm2 ($35 < \phi_m < 55°$). Thus, as the interface

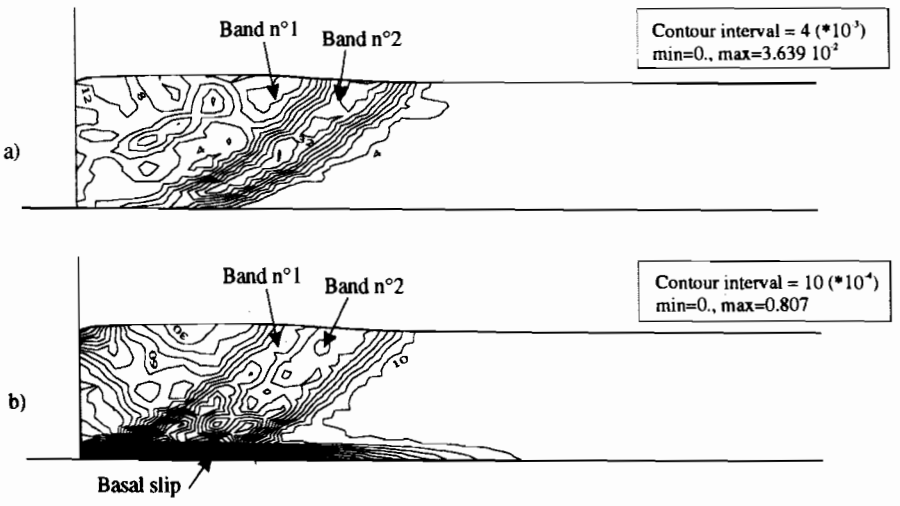

Fig. 10. Isovalues maps for simulation 3 at $u = 0.2$ cm. (**a**) Kinematic indicator α. (**b**) Equivalent strain: higher strain values are located along the basal slip.

friction angle corresponds to 45°, plastic failure preferentially occurs in the sand massif instead of occurring along the frictional interface.

Additional differences with sm1. Another difference can be expected between sm3 and sm1: as mobilized friction angle is lower here than in sm1, sm3 model should b e less resistant than sm1. This is in fairly good agreement with finite element results obtained at $u < 0.129$ cm: the horizontal reaction is found to be slightly lower for sm3 than for sm1 (see Fig. 5).

However the Lode angle influence has even induced more subtle differences between sm1 and sm2, i.e. some important changes in the stress path followed. Figures 11a–b present, in the deviatoric plane, the stress paths followed by the 3 points A, B and C (previously located on Fig. 8) between $u = 0$ and $u = 0.2$ cm (i.e. prior localization), for simulation 1 and simulation 3 respectively.

In the first stages, in both cases the stress paths are close to the hydrostatic axis and follow triaxial compression ones: this is quite normal as at the beginning of computation, σ_1 is vertical and $\sigma_2 = \sigma_3$ are horizontally oriented.

As the loading increases, the stress paths for sm1 and sm3 are no longer similar as shown in the deviatoric plane (see Fig. 10a–b): there is an important stress rotation in sm1 whereas almost none occurs in sm3, and the σ_1 and σ_2 components are greater in sm1 than in sm3. These differences might be explained as follow considering the left part of the model: for the two simulations, $\sigma_1 \approx \sigma_x$ is almost horizontal (see Fig. 8a–b), $\sigma_3 \approx \sigma_v$ is vertical and constant due to the body forces (see equation (28)); as the loading increases, σ_1 and σ_2 will increase by moving onto the yield surface; however the different shapes of the two yield surfaces with σ_3 constant will lead to different stress paths and stress states, which will result in a higher increase of σ_1 and σ_2 in sm1 than in sm3 and thus which will traduce in a larger rotation of stress path in deviatoric plane for sm1. This important change in stress distribution can be seen clearly on Figs 11c–d showing the evolution of the stress shape factor R_S

$$R_S = \frac{\sigma_2 - \sigma_1}{\sigma_3 - \sigma_1} \quad (\text{with } 0 < R_S < 1) \qquad (31)$$

and for which the R_S values are lower in sm1 (Fig. 11c) than in sm3 (Fig. 11d).

As a result, the predicted type of faulting at a given loading will be different in the two cases. For instance at $u = 0.2$ cm and according to the classification given in Sassi & Faure (1995), in sm1 the faulting would consist of pure reverse faulting, whereas in sm3 it would rather consist of a

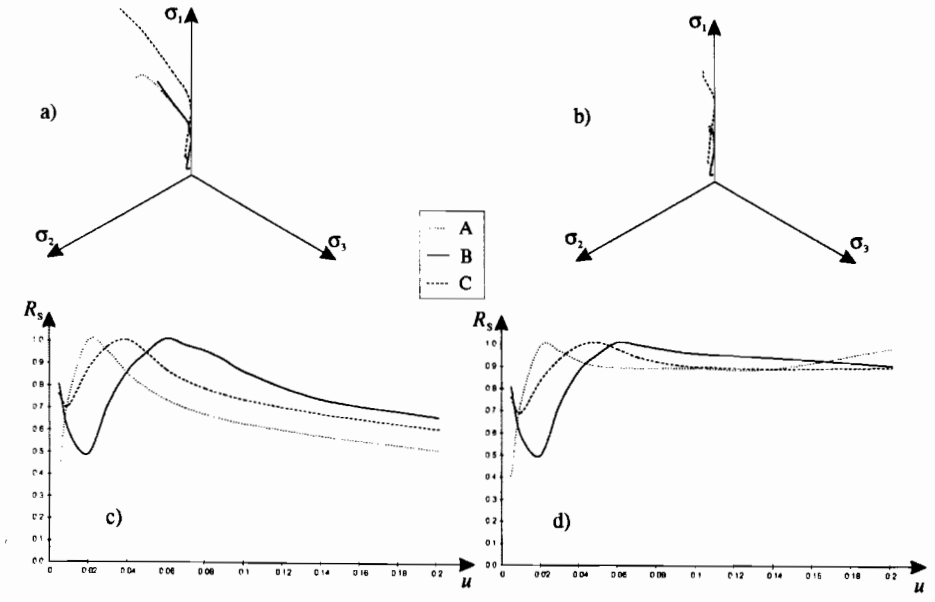

Fig. 11. Stress path and shape ratio for points A, B and C, for $0 < u < 0.2$ cm (for exact location, refer to Fig. 8). **(a, b)** Stress paths in the deviatoric plane for simulation 1 and simulation 3, respectively. **(c, d)** Stress shape ratio, R_S, versus horizontal displacement, u, for simulation 1 and simulation 3, respectively.

combination of reverse strike-slip and pure reverse faulting.

Thus the influence of the Lode angle in the constitutive relation is non-negligible on the stress path and on the stress shape ratio R_S, which might be of some importance when these are used to interpret faulting regimes (Sassi *et al.* 1993; Sassi & Faure 1995).

Comparison with analogue experiments

Although a very large number of physical experiments have been performed using sandbox models, it is only recently that the computer assisted tomography has improved significantly the amount of information which can be obtained from these experiments. One of the published experiments (Colletta *et al.* 1991) is of great interest here as the initial geometry used is almost identical to the one described in Fig. 3. However, the loading displacement values at which experimental results are given ($u = 3.6$ cm) are much higher than in the numerical simulations performed here ($u = 0.9$ cm for sm1).

The structural interpretation of the physical experiment and the present numerical simulation 1 is presented on Figs 12a–b: fault locations are built in the first case from computed tomography pictures (Colletta *et al.* 1991) and in the second case from the cumulated equivalent strain for $0 < u < 0.9$ cm (summation of values given in Figs 4a, b, c).

Strong similarities exist between the physically observed and numerically predicted structures: in both cases some imbricated forward thrusts develop in front of the left boundary whereas one backthrust develop close to the left boundary. The foreland migration of thrusting observed by Colletta et al. (1991) is also observed here as band n. 1 develops prior band n. 2. The pop-up structure observed is in front of the thickened wedge is not present here due to the smallest amount of applied displacement.

Conclusion

The three numerical simulations of a sandbox compression experiment performed in this study lead to several comments.

Two simulations performed using a 'classical' Drücker–Prager yield criterion lead to the formation of several shear bands, which can be interpreted as reverse faults (forward thrusts and backthrusts). Especially the phenomenon of localization could be followed in a very attentive way using Rice criterion and a kinematic indicator, which enable the second order bands associated with shear band competition to be visualized. The orientation of those shear bands is compatible with theoretical predictions; the backthrust dip is found greater than the forward one, which is explained by the clockwise rotation of principal stresses induced by the basal shear. A comparison with a similar sandbox experiment shows that numerical displacement fields and shear band localization are in fairly good agreement with what is observed in experiments.

An interesting feature is that a structural (or geometrical) softening in the force/displacement curve could be observed even if no softening was introduced in the constitutive relation.

The effect of initial stress state has been checked using two different values for the horizontal/vertical stress ratio K_0. Results show that, for the hydrostatic ($K_0 = 1$) and the deviatoric ($K_0 = 0.25$) state of stress, the resulting displacement fields and shear band localization are almost identical; the main difference consists only in the slightly lower displacement required to obtain bifurcation in the hydrostatic case compared with the deviatoric one.

Regarding the friction angle effects, some significant differences between Drücker–Prager and Van Eekelen criterion are observed: (a) Drücker–Prager model in which extension friction angle is excessively high (e.g. $\phi_E = 68°$ if $\phi_C = 35°$) leads to an overestimation of the sand resistance, which results in an overestimation of forces, (b)

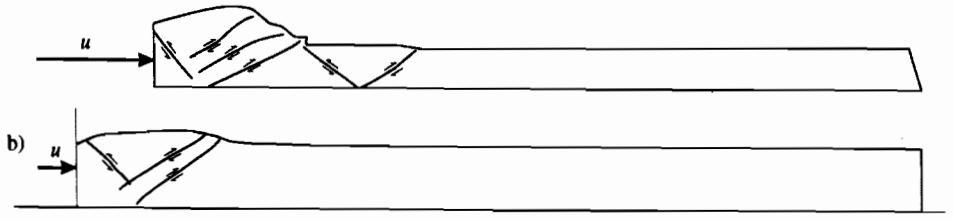

Fig. 12. (**a**) Structural interpretation of thrust propagation experiments performed on sandbox models at $u = 3.6$ cm (adapted after Colletta *et al.* 1991): three imbricated forward thrusts have developed close to the vertical boundary, with only one associated backthrust. A new pop-up structure starts to develop in the foreland at the right part of the thickened wedge. (**b**) Structural interpretation from cumulated equivalent strain for numerical simulation 1 at $u = 0.9$ cm: two imbricated forward thrusts and one backthrust have developed.

strain localization occurs in both cases, although an additional basal slip plane develops in the VE model due to the relative friction angle between the sand and interface, (c) the 2 models lead to very different stress paths and thus may lead to a quite strong modification the stress shape ratio, which has a non-negligible influence when faulting analysis based on the stress shape factor is performed.

Clearly the Van Eekelen criterion seems a quite promising criterion for simulation of frictional material as sand. It is also worth pointing out that this criterion actually does not necessarily require laboratory identification of any additional material parameters as ϕ_E becomes an explicit parameter, whereas ϕ_E is a hidden one in the Drücker–Prager criterion.

Further investigations should show the effect of other parameters (basal friction, cohesion, elastic module) on the Lode angle, the position and orientation of faults. In that sense, a kind of inverse analysis of the significant material parameters could be done. Some improvements of the finite elements with regards to localization should be incorporated in such analysis in the future (see e.g. Wang 1993). Three dimensional aspects and hydromechanical coupling and other localization considerations could also be analysed in future work.

The authors thank Jean Chéry, Dick Nieuwland and an anonymous reviewer for their critical comments on the first manuscript. Dominique Fourmaintraux who initiated this project and the research group Geofrac (Elf Aquitaine, Institut Français du Pétrole and Total, which gives permission for publication are also gratefully acknowledged).

References

ARTHUR, J. R. F., DUNSTAN, T., AL-ANI, Q. A. J. L. & ASSADI, A. 1977. Plastic deformation and failure in granular media. *Géotechnique*, **27**, 53–74.

CESCOTTO, S. 1989. General strategy for non-linear finite element formulation. *In*: GRUBER, R. *et al.* (eds) *Proceedings of the 5th International Symposium on Numerical Methods in Engineering*. Springer Verlag, **1**, 155–164.

—— & CHARLIER, R. 1993. Frictional contact finite elements based on mixed variational principles. *International Journal for Numerical Methods in Engineering*, **36**, 1681–1701.

——, HABRAKEN, A. M., RADU, J. P. & CHARLIER, R. 1989. Some recent developments in computer simulation of metal forming processes. *Proceedings of the 9th International Conference on Computer Methods in Mechanics*, **4**, 19–52, Krakow-Rytrov, Poland.

CHARLIER, R. & CESCOTTO, S. 1988. Modélisation du phénomène de contact unilatéral avec frottement dans un contexte de grandes déformations. *Journal de Mécanique Théorique et Appliquée*, special issue, Suppl. **1**, 7.

CHARLIER, R. & HABRAKEN, A. M. 1990. Numerical modelisation of contact with friction phenomena by the finite element method. *Computers and Geotechnics*, **9**, 1 & 2.

CHENG, C. H. 1988. Automatic adaptive remeshing for finite element simulation of forming processes. *International Journal for Numerical Methods in Engineering*, **26**, 1–18.

COLLETTA, B., LETOUZEY, J., PINEDO, R., BALLARD, J. F. & BALE, P. 1991. Computerized X-ray tomography analysis of sandbox models: examples of thin-skinned thrust systems. *Geology*, **19**, 1063–1067.

DE BORST, R. 1992. Gradient-dependent plasticity: formulation and algorithmic aspects. *International Journal for Numerical Methods in Engineering*, **35**, 521–539.

—— 1993. A generalisation of J_2-flow theory for polar continua. *Computer Methods in Applied Mechanics and Engineering*, **103**, 347–362.

—— & SLUYS, L. J. 1991. Localisation in a Cosserat continuum under static and dynamic conditions. *Computer Methods in Applied Mechanics and Engineering*, **90**, 805–827.

DESAI, C. S. & SIRIWARADANE, H. J. 1984. *Constitutive laws for engineering materials with emphasis on geologic materials*. Prenctice-Hall.

DESRUES, J. 1984. *La localisation de la déformation dans les matériaux granulaires*. PhD Thesis, USMG & INPG Grenoble.

DRÜCKER, D. C. & PRAGER, W. 1952. Soil mechanics and plasticity analysis or limit design. *Quarterly Applied Mathematics*, **10** (2), 157–165.

HABRAKEN, A. M. & CESCOTTO, S. 1990. An automatic remeshing technique for finite element simulation of forming processes. *International Journal for Numerical Methods in Engineering*, **30**, 1503–1525.

MÄKEL, G. & WALTERS, J. 1993. Finite-element analyses of thrust tectonics: computer simulation of detachment phase and development of thrust faults. *Tectonophysics*, **226**, 167–185.

MANDL, G. & SHIPPAM, G. K. 1981. Mechanical model of thrust sheet gliding and imbrication. *In*: *Thrust and Nappe Tectonics*, Geological Society, London, Special Publication, **9**, 79–97.

MATSUOKA, H. & NAKAI, T. 1982. A new failure condition for soils in three-dimensional stresses. *Proceedings IUTAM Conference Deformation and Failure of Granular Materials*, Delft, 253–263.

ORTIZ, M., LEROY, Y. & NEEDLEMAN, A. 1987. A finite element method for localized failure analysis. *Computer Methods in Applied Mechanics and Engineering*, **61**, 189–214.

RICE, J. R. 1976. The localisation of plastic deformation. *In*: KOITER, W. (ed.) *Theoretical and Applied Mechanics*. North-Holland.

SASSI, W. & FAURE, J. L. 1995. Role of faults and layer interfaces in the spatial variation of stress regime in basins: inference from numerical modelling, *Tectonophysics*, in press.

——, COLLETTA, B., BALÉ, P. & PAQUREAU, T. 1993. Modelling of structural complexity in sedimentary basins: the role of pre-existing faults in thrust tectonics. *Tectonophysics*, **226**, 97–112.

SCHWEIGER, H. F. 1994. On the use of Drücker–Prager failure criteria for earth pressure problems. *Computers and Geotechnics*, **16**, 223–246.

VAN EEKELEN, H. A. M. 1980. Isotropic yield surfaces in three dimensions for use in soil mechanics. *International Journal for Numerical and Analytical Methods in Geomechanics*, **4**, 98–101.

VILOTTE, J. P., POZZI, J. P., PHILIPPE, C., PASTOR, M., ZIENCKIEWICZ, O. C., DAUDRE, B. & BARDES, P. 1990. Modes localisés de la déformation dans les matériaux crustaux. *Rapport scientifique, GRECO Géomatériaux.*

WANG, X. 1993. *Modélisation numérique des problèmes avec localisation de la déformation en bandes de cisaillement.* PhD thesis, Université de Liège, Faculté des Sciences Appliquées.

ZIENKIEWICZ, O. C. & ZHU, J. Z. 1987. A simple error estimator and adaptive procedure for practical engineering analysis. *International Journal for Numerical Methods in Engineering*, **24**, 337–357.

ZIENCKIEWICZ, O. C. & TAYLOR, R. L. 1988. *The finite element method* (4th edn), MacGraw-Hill Book Company.